# Enhanced Anisotropic Scattering Targets Imaging in Wide-Angle SAR

**Xin Wang**[*]**, Guiqing Chang, and Chenchen Chi**

**Abstract**—In wide-angle synthetic aperture radar (SAR), the scattering behavior of many illuminated objects might vary with the observation angle, which results in the degradation of the resolution and interpretability of the reconstructed imagery. To solve this problem, a sparse-based methodology is proposed in this paper to implement the separation of the anisotropic scattering target data and imaging processing simultaneously. The distinct reflection characteristics of the illuminated targets are employed to formulate a composite projection operator. Then, the sparse constraint is utilized to suppress cross-projection energy. Finally, the imagery of the anisotropic scattering targets could be derived with improved focal quality and interpretability. Numerical simulations could verify the validity of the proposed methodology.

## 1. INTRODUCTION

As an advanced remote sensing system, synthetic aperture radar (SAR) [1, 2] has been widely used in the past decades, whereas it is found that the azimuth resolution of the SAR system with the traditional linear flight path is limited by the data observation angle when the researchers try to further improve the performance of imaging. The idea of wide-angle observation [3–5] is thus proposed in recent years and employed to formulate a larger synthetic interval. In this case, the azimuth resolution could be improved efficiently, which is very useful for target classification, recognition, and location.

However, the scattering of most of the artificial and natural objects is not persistent under a wide viewing angle [6, 7]. The reflector geometry, shadowing, and coherent scintillation might cause the radar reflectivity that is strongly dependent on the aspect angle [8]. The resolution of the reconstructed imagery by the conventional imaging algorithms will be affected. Additionally, the aspect dependent scattering characteristic of targets may be submerged by coherent speckles [9], which is unfavorable for SAR image interpretation and target recognition.

As we know, the anisotropic scattering might be homogeneous in a smaller data collection interval [10]. The sub-aperture approach [11–13], in which the whole observation interval is divided into several smaller apertures, is thus developed for wide-angle SAR data. A group of coarse-resolution images indexed on both the location and azimuth observation angle will be obtained, and the concept of SAR video [14, 15] is proposed. Nevertheless, the reflectivity information in one sub-image is not sufficient. In order to derive one composite SAR imagery, the generalized likelihood ratio test (GLRT) method [16, 17] is developed, where the sub-aperture contribution with the dominant scattering energy is retained while the others are deleted. After GLRT processing, the interpretability of SAR imagery is improved. However, the non-persistent scattering characteristics are not considered in the above algorithms. The decomposed sub-aperture interval is designed to be a fixed value, which might not be synchronous with the real reflection behavior of the illuminated targets. Though scattering intervals determine the theoretical values of resolutions, the real values are in fact limited by the observation intervals of sub-apertures.

* Corresponding author: Xin Wang (wangx@njupt.edu.cn).
The authors are with the Nanjing University of Posts & Telecommunications, China.

To improve the resolution of the reconstructed imagery, the regularization constraint [18, 19] and nonlinear sharpening techniques [20, 21] have been discussed and utilized for wide-angle SAR imaging, respectively. However, the scattering information is still not employed and the reconstructed results are not satisfying. The Bayesian inversion [22], approximate message passing [23], and over-complete dictionary methods [24] are also developed to implement wide-angle SAR imaging. In the Bayesian inversion method, the variance of radar reflectivity of targets is viewed as a dynamic state, and the dynamic Bayesian compressed sensing algorithm is employed to find the solution. The variant scattering reflection is also indicated as the sparse representation of the dictionary composed of basis vectors with varying levels of angular persistence. Nevertheless, the computational burden of these algorithms is expensive.

Besides, the reflected data from the persistent and non-persistent scattering objects are mix-received in radar systems. Owing to their distinct scattering characteristics, different imaging processing filters should be designed. It is thus better to perform data separation before imaging. However, it is challenging, especially in dense scene cases. Moreover, the strong reflection information under some observation angle will mask the weak field information during the other collection intervals, and degrade the interpretability of imagery. In this paper, we propose a sparse-based method to realize the separation and imaging in one channel wide-angle SAR simultaneously. The scattering characteristic estimated in the post-imaging procedure is utilized as feedback to help to formulate the radar projection operator. The sparse constraint, which has been used to implement inverse imaging under down-sampling [25–27], is employed here to promote the separation of SAR data. By using our method, the resolution of the derived imagery will not just be limited by the data collection interval of sub-apertures but improved to be determined by the scattering behavior. Moreover, the interpretability is also ameliorated, which is useful for the following target detection and recognition operations.

The general SAR data collection geometry and signal model are described in Section 2 firstly. Then, the separation and imaging methodology is presented and discussed in Section 3. Finally, numerical simulation verifies that the algorithm can implement the separation and imaging of anisotropic scattering targets simultaneously.

## 2. ANISOTROPIC SCATTERING SIGNAL MODEL

As described in [28–30], the reflectivity of anisotropic scattering targets additionally depends on the aspect angle $\theta$ and frequency $f$ except for the spatial coordinates. However, since the frequency bandwidth is typically much smaller than the carrier frequency in realistic SAR system, it is reasonable to assume that the frequency variation of the scattering centers is very small within the bandwidth. Based on the above assumptions, the received data from the non-persistent targets are expressed as

$$S_a\left(x_a, y_a, \tau, \theta\right) = \sigma_t\left(x_a, y_a, \theta\right) S_r\left(\tau - \frac{2}{c}R\left(\theta\right), \theta\right) \exp\left[-j\frac{4\pi f_c}{c}R\left(\theta\right)\right] \tag{1}$$

where $S_r(\cdot)$ is referred to as the transmitted signal; $\tau$ is the range time; $R(\theta)$ indicates the instantaneous slant range from the target to radar platform with an aspect angle $\theta$; $c$ is the speed of light; and the reflectivity $\sigma_t(x_a, y_a, \theta)$ is variant with the aspect angle.

After matched filtering (MF) processing, the impulse response function (IPR) of the anisotropic scattering targets can be derived as

$$\begin{aligned} y_I\left(x_a, y_a\right) &= S_a\left(x_a, y_a, \tau, \theta\right) \otimes H_I\left(\tau, \theta\right) \\ &= \left[\sigma_t\left(x_a, y_a, \theta\right) \cdot S_r\left(\tau - \frac{2}{c}R\left(\theta\right), \theta\right) \exp\left[-j\frac{4\pi f_c}{c}R\left(\theta\right)\right]\right] \otimes H_I\left(\tau, \theta\right) \end{aligned} \tag{2}$$

where the operator $\otimes$ denotes the two-dimensional convolution operation of radar data with the inverse imaging filter $H_I(\tau, \theta)$. When the scattering behavior is invariant with azimuth aspect angle $\theta$, a two-dimensional sinc-function will be obtained after imaging processing in Eq. (2). Whereas the actual values of $\sigma(\theta)$ for non-persistent scattering targets change with the aspect angle, the derived IPR $y_I(x_a, y_a)$ becomes the convolution of $\sigma_t(x_a, y_a, \theta)$ and the two-dimensional sinc-function. The main lob bandwidth might be extended, and the amplitude of side lobe is increased. In this case, it is difficult to extract the real appearance of the targets, and new imaging processing method should be designed.

## 3. SEPARATION AND IMAGING OF ANISOTROPIC SCATTERING TARGETS

To construct the anisotropic target imagery with high focal quality, the variant scattering behaviors should be considered in the imaging procedure. However, as described in Section 2, the radar cross-section (RCS) information is space- and time-variant, which implies that the ideal imaging processing of wide-angle SAR data needs a bank of matched filters with different lengths and weighting parameters. The computational burden will be very expensive. Moreover, the reflection from the non-persistent scattering targets is mix-received with that from the persistent scattering targets. It is better to perform data separation in advance since different imaging processing filters are needed.

In this section, a sparse-based separation and imaging method will be proposed, where the different reflection behaviors of the isotropic and anisotropic scattering targets are exhibited in one composite radar system matrix $F = [F_p, F_d]$. The matrixes $F_p \in \mathbb{C}^{N_d \times N_I}$ and $F_d \in \mathbb{C}^{N_d \times N_I}$ are referred to as the radar projection operators of the persistent and non-persistent scattering targets. After range compression, the radar back data can be expressed as [27]

$$S = F_p f_p + F_d f_d + n_0 = F \begin{bmatrix} f_p \\ f_d \end{bmatrix} + n_0, \tag{3}$$

where $S \in \mathbb{C}^{N_d \times 1}$ is the column vector derived by stacking the received SAR data. In the radar system matrix $F = [F_p, F_d]$, the $i$th column vectors of $F_p$ and $F_d$ are derived by stacking the SAR system functions of the target located at the $i$th element in $f_p$ and $f_d$. Moreover, the notations $N_d$ and $N_I$ are referred to as the length of SAR data and imagery. The subscripts $p$ and $d$ correspond to the iso- and anisotropic objects, and $n_0$ denotes the noise vector.

Generally, the analytical expression of $F_p$ can be produced exactly according to the radar system parameters while the matrix $F_d$ is difficult to derive. Seeing from Eq. (1), we find that the aspect-angle-variant scattering characteristic could be viewed as an amplitude weighting matrix of the received radar data. The projector $F_d$ could thus be expressed as

$$\widehat{F_d} = F_p \widehat{A}, \tag{4}$$

where $\widehat{A} = \mathrm{diag}\{A_i\}$ is a diagonal matrix consisting of the additional weighting information of the IPR, which is introduced by the anisotropic scattering behavior. Owing to the diverse scattering characteristics, the coherence relationship between radar back data from the persistent and non-persistent scattering targets and system matrixes $F_p$ and $F_d$ are different. We could realize the separation by using a sparse norm constraint on the solution of Eq. (3). The following optimization function is formulated

$$\arg \min_{f_p, f_d} \|S - F_p f_p - F_d f_d\|_2^2 + \lambda_1 \|f_p\|_p^p + \lambda_1 \|f_d\|_p^p, \tag{5}$$

where $\| \cdot \|_p^p$ denotes $\ell_p$ norm, and $\lambda_1$ is positive scaling parameters.

In Eq. (5), the first term is a data fidelity term. As described in Eq. (2), the IRP of the anisotropic target is the convolution of the RCS function and the ideal IPR. When the scattering of the target is not consistent, the azimuth envelope of the received radar signal is interrupted, which finally results in the degradation of image quality. Herein, since the scattering behavior of targets is considered in the optimization problem to compute the projector $F_d$, the distortion of IPR introduced by variant RCS will be removed from the derived image. The anisotropic scattering target imagery $f_d$ could be obtained by solving the optimization problem in Eq. (5).

The second and third terms aim to constrain the solution to be sparse. The $\ell_p$ norm implies a sparse constraint on the solution, which has been widely used in CS processing to recover the down-sampling data successfully. Herein, the utilization of $\ell_p$ norm is viewed as imposing an energy-type constraint on the solutions $f_p$ and $f_d$ [27]. We use the sparse norm condition to realize the separation of the mix-received data, the suppression of artifacts, and the improvement of the resolvability of scatters in the solution. As the correlation relationship between the data from the isotropic and anisotropic targets and the two system matrixes $F_p$ and $F_d$ are distinct, the SAR data will thus be separated to derive two vectors. Most of the energy of the isotropic scattering targets will be concentrated on the derived imagery $f_d$ while the non-persistent objects will be obtained in $f_p$.

During the iterative computation in Eq. (5), coherent addition will be utilized, which means that the resolution of the reconstructed IPR is determined by the real scattering interval of the illuminated targets. In addition, noise and side-lobes will be suppressed as a result of the utilization of the sparse constraint, which is helpful for the improvement of the imagery resolution. After iteration computation, two separate imageries will be obtained.

## 4. ITERATIVE SOLUTION

When the scattering behavior of the illuminated targets is given accurately, the solution of the optimization problem in Eq. (5) could be derived by iterative computation conveniently. However, this is not the case. To provide the essential initialized parameters, the anisotropic scattering characteristic estimation operation should be performed in advance. Considering the time- and space-variance of the reflection behaviors of the illuminated targets, we utilize an aperture decomposition and imagery segmentation strategy to construct $\widehat{F}_d$ and $\widehat{f}_d^{(0)}$. Then, the optimization problem in Eq. (5) is solved by the Quasi-Newton method to derive the imagery.

### 4.1. Initialization

Accurate estimation of the weighting matrix $\widehat{A}$ is generally difficult to realize due to its space- and time-variance. Herein, we calculate it approximately by performing aperture decomposition and segmentation on the space pixels. The sub-aperture method is utilized here to provide a group of images for the estimation of the reflection information. Nevertheless, the existence of strong isotropic scattering targets might affect the estimation of RCS information. In this case, the estimated scattering behavior might deviate from the real values severely and thus affect the separation results, especially in dense scene cases. To solve this problem, we try to use the Low-rank matrix decomposition (LRMD) method to separate the strong persistent targets in advance. After sub-aperture processing, the derived coarse-resolution images could be expressed as

$$S_I = [H_{I1}(f_p + f_{d1}), H_{I2}(f_p + f_{d2}), ..., H_{IK}(f_p + f_{dK})] + n_I, \tag{6}$$

where

$$S_I = [S_{I1}, S_{I2}, ..., S_{IK}],$$

In Eq. (6), the matrix $H_{Ii} \in \mathbb{C}^{N_I \times N_I}$ is referred to as the inverse imaging operator, where the subscript $i$ corresponds to the $i$th sub-aperture; $K$ is the number of sub-apertures; the column vector $f_{di} \in \mathbb{C}^{N_I \times 1}$ denotes the filed information of the non-persistent targets during the sub-aperture observation intervals; and $n_I$ denotes the noise vector in the imagery.

Since the isotropic reflection is persistent during the whole aperture interval, it could be viewed as the low rank components of the derived sub-imageries. Theoretically, LRMD could be utilized to extract the imagery patches of persistent objects. However, the variance of radar projection operators $F_i$, which will interrupt the low rank property of images of persistent scatters, is not considered in these methods. Besides, when the locations of the scattering center of the anisotropic targets do not change with the observation angle, the non-persistent objects will also remain in the derived low rank components. Thus, the results obtained via traditional LRMD and robust principle components analysis (RPCA) methods are generally not satisfactory.

Considering that the main purpose of the pre-separation is to reduce the energy of the isotropic targets, we can still use the LRMD method herein to derive the low-rank part $f_p$ and sparse part of $f_{di}$. A threshold function $\upsilon(\cdot)$ is used to limit the sparse solution and avoid the emergence of false targets. The elements, of which the amplitude is larger than the original sub-aperture imagery $S_{Ii}$, are deleted.

After pre-separation, the estimation of the RCS function will be less affected by the isotropic targets. The sparse images $\widehat{f}_{di}(i = 1, 2, ..., K)$ are coherently integrated to produce the initialization of non-persistent image as

$$\widehat{f}_d^0 = \sum_{i=1}^{K} \widehat{f}_{di} \Big/ \widehat{A}_i, \tag{7}$$

where $\widehat{f}_{di}\,(i = 1, 2, ..., K)$ denotes the estimated sparse part of the sub-image $S_{Ii}$, and $\widehat{A}_i$ is the estimated RCS amplitude information of the extracted scatter center in sub-image $S_{Ii}$.

The scatter centers are extracted, and image segmentation is performed, where the amplitude information of the extracted scatters is used to formulate $\widehat{f}_d^{\,0}$ and $F_d$ approximately. It is obvious that the decomposition of sub-aperture and segmentation of imagery will affect the interpretability of the reconstructed solution. Smaller aperture intervals will result in the vibration of the estimated values of $\widehat{A}_i$ while larger synthetic aperture might include some strong reflections, which will mask the other weak scattering energy. Suitable sub-aperture decomposition will help to derive accurate RCS estimation and reconstruct imagery with high interpretability.

However, it is not easy to give a quantitative criterion about how to decompose the whole aperture. In our numerical simulations, we find that it is better to design the sub-aperture decomposition scheme according to the scattering behaviors of the illuminated targets or relative orientations of the illuminated targets to radar. The observation interval, during which the scattering behaviors of targets are approximately invariant or the radar platform locates on the same side of the targets, is synthesized as one sub-aperture. During one sub-aperture, high similarity exists in the derived images, which could be measured by the correlation coefficients. To obtain the aperture decompose scheme, we could divide the whole observation interval into several very small apertures firstly. Since the observation angle intervals of the decomposed aperture are very small, the scattering behaviors could be viewed as invariant, and coarse resolution images are derived. Then, the commonly used clustering method is employed to design the grouping schemes and formulate the radar projection operator approximately. Based on this decomposition scheme, subintervals during which the scattering of the targets changes slightly will be classified into one cluster. The weighting matrix will help to separate the mix-received data and balance the contribution of the reflection energies, and thus the interpretability of the finally derived imagery will be improved.

## 4.2. Iteration Computation

There are two unknown parameters in the optimization problem in Eq. (5). After denoting $f = [f_p, f_d]^T$ and substituting the approximation of $\ell_p$ norm [18], we could simplify the solution procedure of Eq. (5) as

$$\min J_{0m}\,(f) = \min_f \left\| \bar{F}^H S - \bar{F}^H F f \right\|_2^2 + \lambda \sum_{i=1}^{N_I} \left( |f(i)|^2 + \varepsilon \right)^{p/2} \tag{8}$$

where $\varepsilon \geq 0$ is a small positive constant, and $\bar{F}^H$ denotes the inverse imaging projector. As the variant scattering behavior is compensated in the initialization in Eq. (7), $\bar{F}$ is denoted as $[F_p, \widehat{A}^{-1} F_p]^T$, where the diagonal matrix $\widehat{A}$ is estimated by the operations in Section 4.1. Herein, a common scaling parameter $\lambda$ is used instead of restricting the sparse characteristics of $f_p$ and $f_d$ to simplify the solution procedure, respectively. Calculating the gradient of Eq. (8) to the real part and imaginary part of $F$, we can obtain the following iterative formula based on the Hessian matrix approximation [27]

$$\left[ H\left( \widehat{f}^{(n)} \right) \right] \widehat{f}^{(n+1)} = 2\gamma \bar{F}^H S, \tag{9}$$

where

$$H\left( \widehat{f}^{(n)} \right) \triangleq 2\bar{F}^H F + p\lambda_1 \text{diag}\left\{ \left( \left| \widehat{f}^{(n)}(j) \right|^2 + \varepsilon \right)^{p/2-1} \right\}, \tag{10}$$

In Eq. (9), $\gamma$ denotes the iteration step, and $\widehat{f}^{(n)}$ is the estimation result after the $n$th iteration. It can be seen from Eq. (9) that it is actually a linear equation with conjugate matrix coefficients. The sparsity of the coefficient matrix is increased by neglecting elements in $H(\widehat{f}^{(n)})$ whose magnitudes are very small. Hence, the conjugate gradient iterative threshold method could be applied to search for the

solution of Eq. (9). Since the radar system projection operator and variant scattering characteristics are both incorporated in the iterative computation, the above steps could not only realize the separation of data but also implement imaging processing. The derived solution can be restacked to obtain the imageries of the anisotropic scattering and isotropic scattering targets simultaneously, and the detailed processing flow is given in Fig. 1. Then, we will compare the computational cost of our processing and the over completed dictionary method. Assuming the dimensions of SAR data and imagery are both $N \times N$, the number of the elements in the solution is $2N^2$, and the complexity of our processing is of the order $O(2N^4)$. In the over completed dictionary method, the amount of the elements in the dictionary is designed as $MN^4$, where $M(M \gg N)$ is the number of basis vectors. The length of the derived solution is of the order $o(N^3)$, and the complexity is of the order $o(N^6)$, which is restrictive in terms of memory and computation. By contrast, the computational burden and memory requirement of our processing are both reduced effectively.
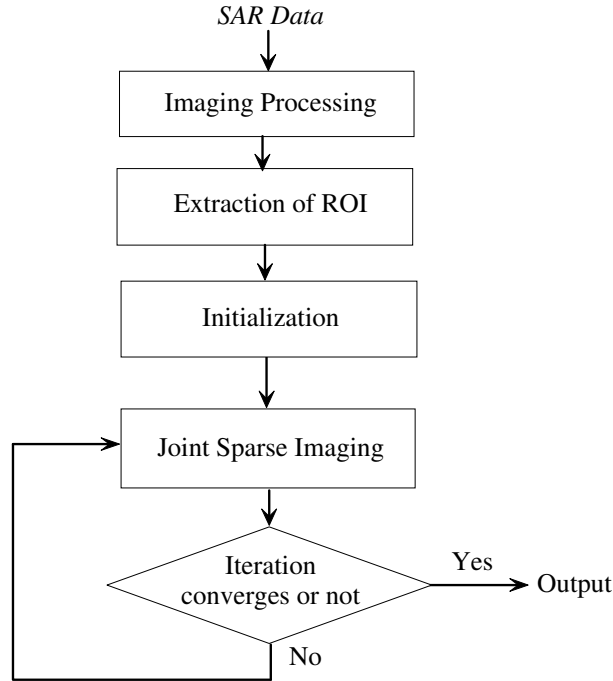


**Figure 1.** Joint sparse imaging processing flow.

## 5. EXPERIMENTAL RESULTS

In this section, experiments with different configurations will be performed to prove the validity of our algorithms. Firstly, point target simulation is implemented via the processing flow in Fig. 1, in which several non-persistent targets with invariant and variant scattering centers are employed, respectively. Then, the Backhoe data from Air Force Research Laboratory (AFRL) will be processed to reconstruct SAR imagery with high interpretability. The data set is recorded from electromagnetic simulation and consists of simulated wideband (7–13 GHz), full polarization, and complex backscatter data from a backhoe vehicle in free space. The observation angle interval is 110°. Due to the wide angle observation geometry, the imagery derived by traditional full aperture processing will suffer severe degradation. In the following discussion, the detailed experimental setup and results will be given and analyzed to verify the effectiveness of our algorithm.

## 5.1. Point Target Simulation

The simulation parameters are listed in Table 1. The wide-angle SAR data illuminated from the isotropic and anisotropic targets are simulated and processed via the sparse-based method. In the first simulation, 3 anisotropic targets with invariant scattering center combined with 1 isotropic target are employed. The geometry relationship of the simulated PTs and the RCS function is depicted in Figs. 2(a) and (b), respectively. After back-projection processing, the image is reconstructed and given in Fig. 2(c), where the rectangular and circular frames indicate the positions of persistent and non-persistent targets. It could be seen from Fig. 2(c) that the main-lobe width of the IPR of the 3 non-persistent PTs is enlarged as a result of the non-persistent scattering behavior. Herein, the whole aperture is decomposed to obtain two sub-apertures with the aspect angle 90° and 270°, respectively. The positive parameter $\lambda$ is set to 0.15, $\varepsilon = 1^{-5}$ and $p = 0.8$, which are all defined by experience [27]. The coarse-resolution images derived in the two sub-apertures are obtained and given in Figs. 3(a) and (b). In the second sub-aperture, no reflection energy from the anisotropic targets is collected, and thus only 1 isotropic target emerges. The pre-separation results of the two sub-aperture data are given in Figs. 3(c) and (d), where most of the energy from the 2 non-persistent PTs is extracted. After the sparse-based imaging, the imagery of the anisotropic targets is obtained in Figs. 3(e) and (f). It could be seen from these figures that both the isotropic scattering and anisotropic scattering PTs are focused.

**Table 1.** Simulation parameters.

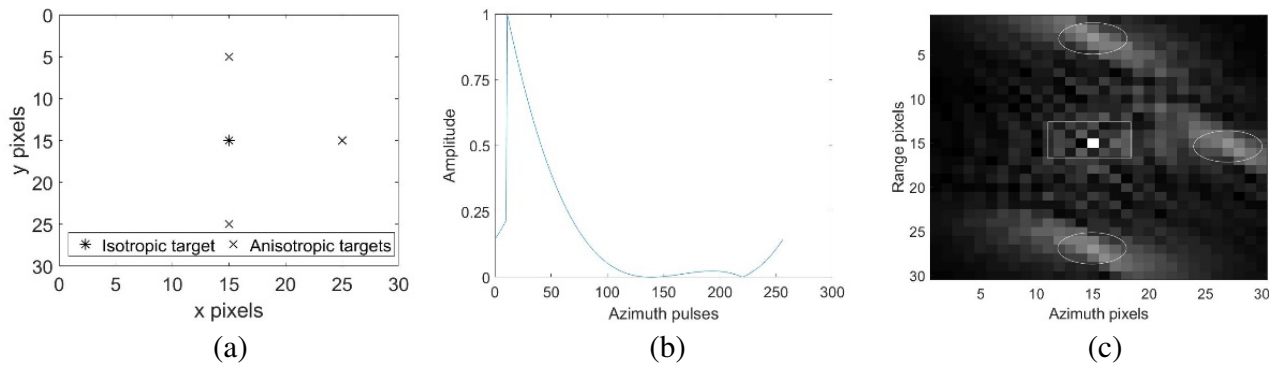| Carrier frequency | 10 GHz |
|---|---|
| Range bandwidth | 500 MHz |
| Slant range | 8000 m |



(a)  (b)  (c)

**Figure 2.** Geometry relationship of the 3 PTs in the first simulation. (a) Geometry relationship of the simulated PTs; (b) RCS function of the 2 anisotropic scattering targets; (c) MF result.

In the second simulation, a circular object with the variant scattering center combined with 24 iso-targets is designed in the simulation. The aperture is decomposed to get four sub-apertures with the aspect angles 45°, 135°, 225°, 315° in the imaging processing. The whole aperture image and sub images are derived and given in Fig. 4(b) and Figs. 5(a)–(d), respectively. It could be seen from Fig. 4(b) that the images are smeared, and the real appearance of the illuminated targets cannot be revealed. Owing to the variant scattering characteristic, the derived sub imageries from the sub-apertures are distinct.

The pre-separation results of the four sub apertures are given in Figs. 5(e)–(h), respectively. Then, the scattering center extraction and RCS estimation operations are performed sequentially, and the radar system operator is reconstructed. The mix-received SAR data are then performed by the sparse-based processing. The derived imageries of the isotropic and anisotropic scattering targets are given in Figs. 6(b) and (c), respectively. In Fig. 6(b), the black cross implies the successfully focused persistent

scattering targets while the red rectangular frames indicate the missed targets. It could be seen from Fig. 4(b) and Fig. 6(a) that the focal quality of the MF and GLRT methods degrades as a result of the existence of the non-persistent scattering targets. The L1 norm constraint can also realize the suppression of side-lobe in the derived imagery. Nevertheless, the non-persistent targets are masked as a result of the low scattering energy. Moreover, LRMD processing could realize data separation while residual cross-projection energy still exists in the derived results. In comparison, our algorithm realizes the separation of data and imaging of anisotropic scattering targets effectively. The energies of the isotropic and anisotropic scattering targets are decomposed and focused, respectively. The iterative numbers under different parameter settings are also discussed and depicted in Fig. 7. It can be seen from



(a)                                        (b)                                        (c)



(d)                                        (e)                                        (f)
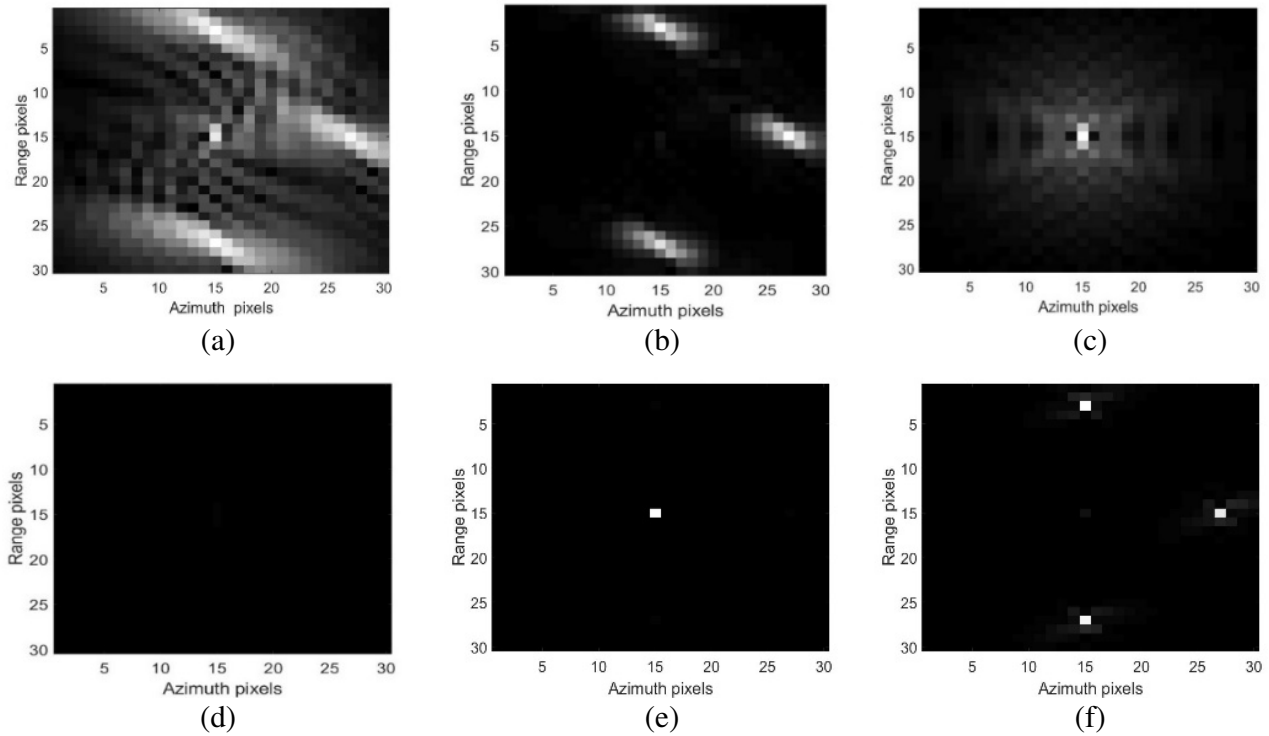
**Figure 3.** Sub-aperture images and pre-separation results. (Note: the scattering center of the 2 anisotropic scattering targets is invariant.) (a) Sub-aperture 1; (b) Pre-separated sparse component of Sub-aperture 1; (c) Sub-aperture 2; (d) Pre-separated sparse component of sub-aperture 2; (e), (f) The sparse imaging results of the isotropic scattering and anisotropic scattering targets.
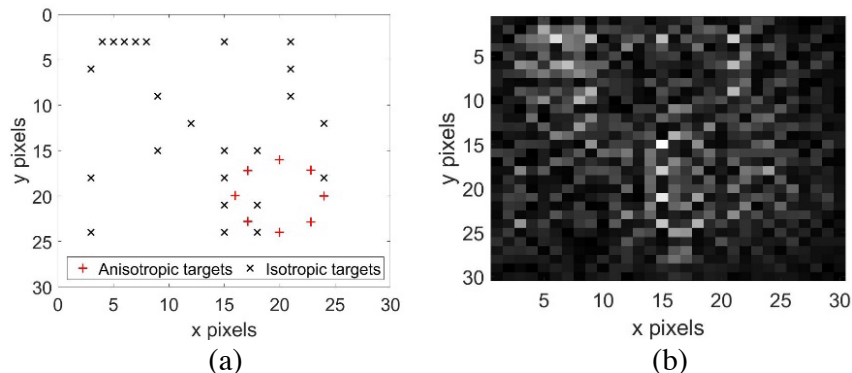


(a)                                        (b)

**Figure 4.** PTs in the second simulation.

Figs. 7(a)–(d) that the derived imageries are different due to variant weighting of the sparse constraint term. The convergence is accelerated with the diminish of $p$ and increase of the scaling parameter $\lambda$ as depicted in Fig. 7(e). However, overfitting might exist in the numerical calculation when the scaling parameter $\lambda$ is too large. Some of the targets might also be suppressed because of the heavy weighting of sparse constraint as depicted in Figs. 7(c)–(d). Herein, empirical values with $\lambda = 0.15$ and $p = 0.8$ are selected, as mentioned earlier, to avoid the above problems.

### 5.2. Backhoe Data Results

In this section, the Backhoe data are processed via coherent matched filtering, GLRT, and our sparse-based processing, respectively. The observation angle width of Backhoe data is $110°$, and the elevation angles are $0°$ and $30°$. Most of the illuminated targets in the data are non-persistent scattering. The imageries derived by the coherent and non-coherent processing are fuzzy with low interpretability, which are depicted in Figs. 8(a)–(c) and (d)–(e). The strong reflection energy under the aspect angle interval $90°$–$110°$ masks the other weak scattering targets, and hence affect the understanding of the image.

In our sparse-based processing, sub-aperture decomposition operation is performed to provide a group of images for initialization. As discussed in [13] and [16], most of the non-persistent scattering targets could maintain the reflection during smaller observation intervals. We thus divide the whole aperture into 19 intervals, each with an azimuth response centered at $0°$, $5°$, ..., $90°$ and width $20°$. After back-projection processing, 19 coarse-resolution images indexed on different aspect angles could be derived.
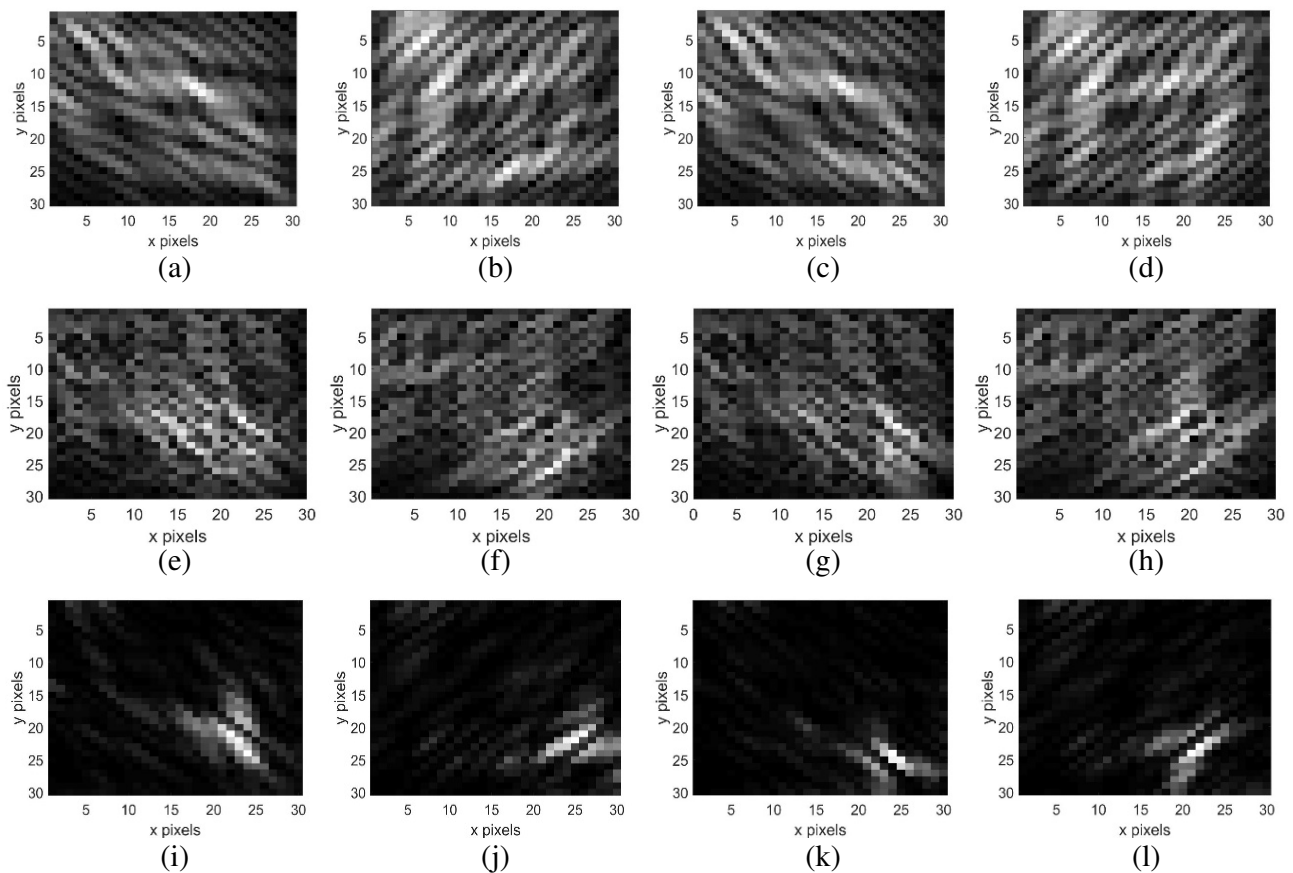


**Figure 5.** Sub-aperture imageries and separation results. (a), (b), (c) and (d) MF results of sub-aperture with aspect angle $45°$, $135°$, $225°$ and $315°$; (e), (f), (g) and (h) Separated anisotropic scattering imagery of sub-apertures.
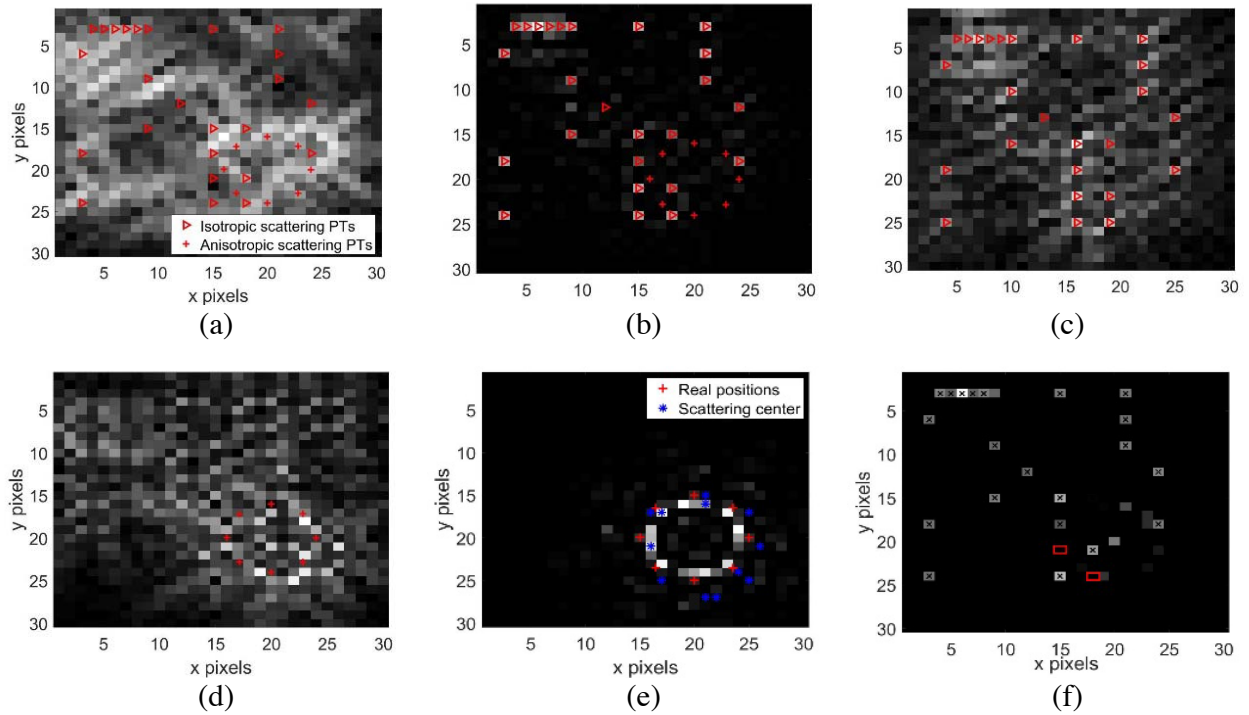
**Figure 6.** Imaging results. (a) GLRT method; (b) L1 norm method; (c) and (d) LRMD results of the persistent and non-persistent scattering targets; (e) and (f) Imageries of the 27 isotropic scattering and anisotropic scattering targets derived by our method. (Note: the scattering center of the extended targets are variant with the aspect angle).
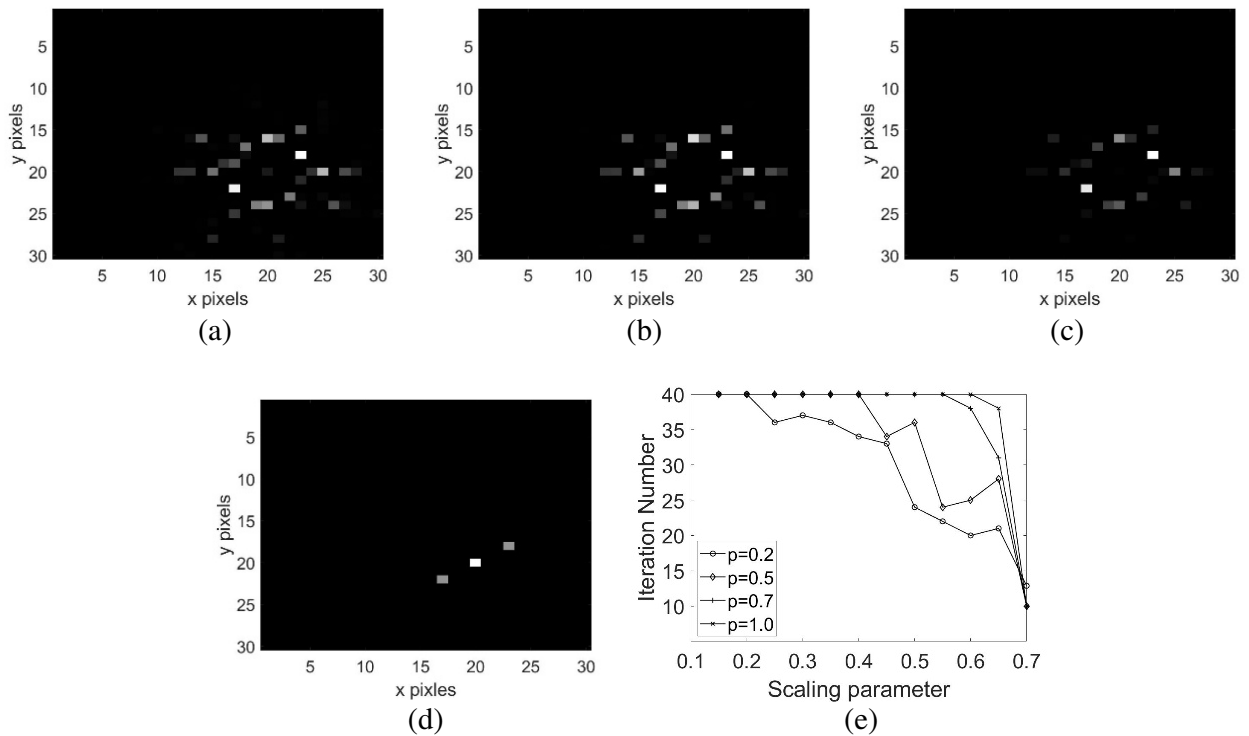


**Figure 7.** Convergence rate of the iteration calculation. (a) $\lambda = 0.2$, $p = 0.8$; (b) $\lambda = 0.2$, $p = 0.5$; (c) $\lambda = 0.4$, $p = 0.8$; (d) $\lambda = 0.4$, $p = 0.5$; (e) Convergence rate with different parameters.

As the scattering of most of the illuminated targets in the data is non-persistent, the separation operation is not performed here. The correlation relationships between any two of the 19 images are investigated, and a simple clustering algorithm is applied. It is obvious that high similarity will exist in some of the coarse resolution images when the scattering of targets is persistent or changes slightly. The correlation distance is utilized here to measure the similarity of images. After clustering, the 19 coarse resolution images are divided into 3 classes, where the results are given in Figs. 8–10. The correlation
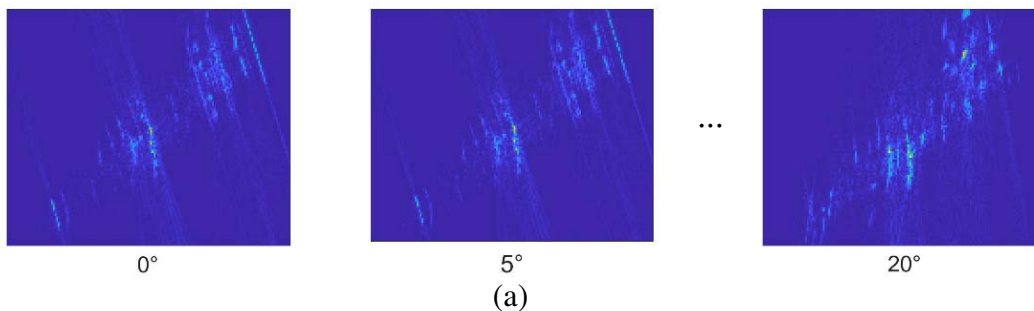


$0°$              $5°$              $10°$

(a)



$15°$              $20°$   ...   $60°$

(b)



$65°$              $70°$   ...   $90°$

(c)
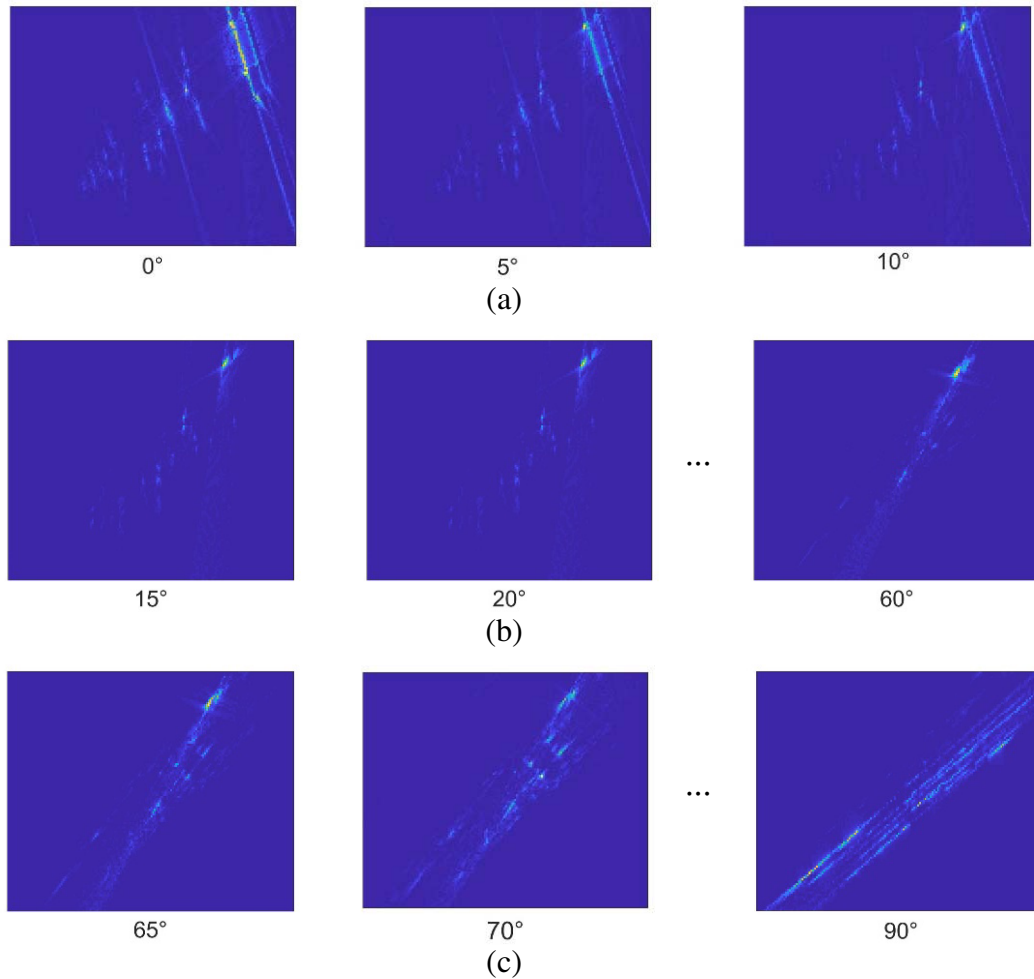
**Figure 8.** Clustering results of the 19 coarse resolution images under elevation angle $0°$. (a) Cluster 1; (b) Cluster 2; (c) Cluster 3.



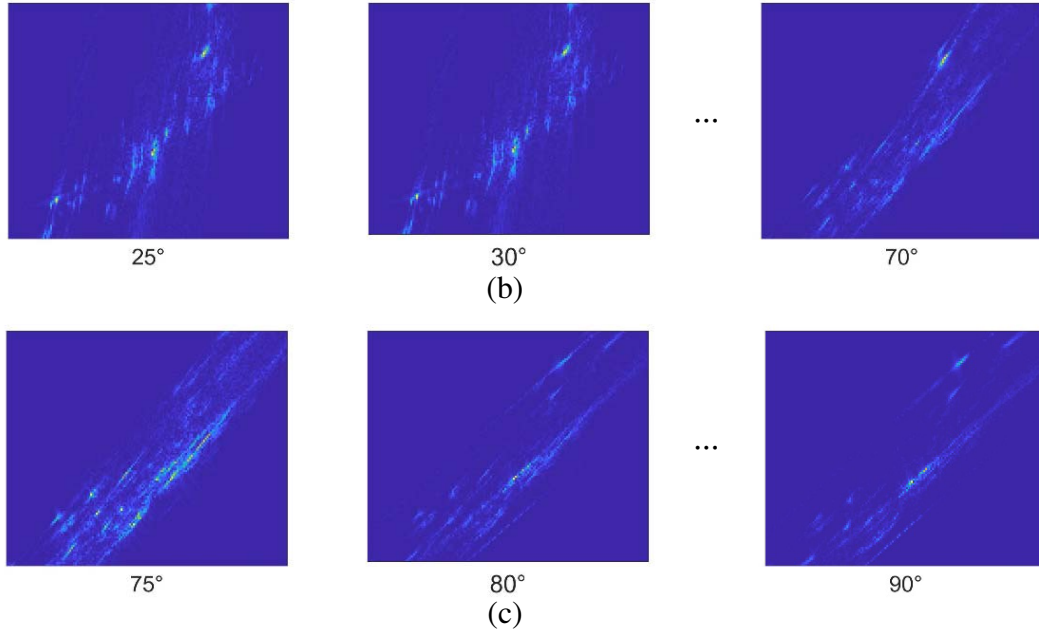$0°$              $5°$   ...   $20°$

(a)

**Figure 9.** Clustering results of the 19 coarse resolution images under elevation angle 30°. (a) Cluster 1; (b) Cluster 2; (c) Cluster 3.
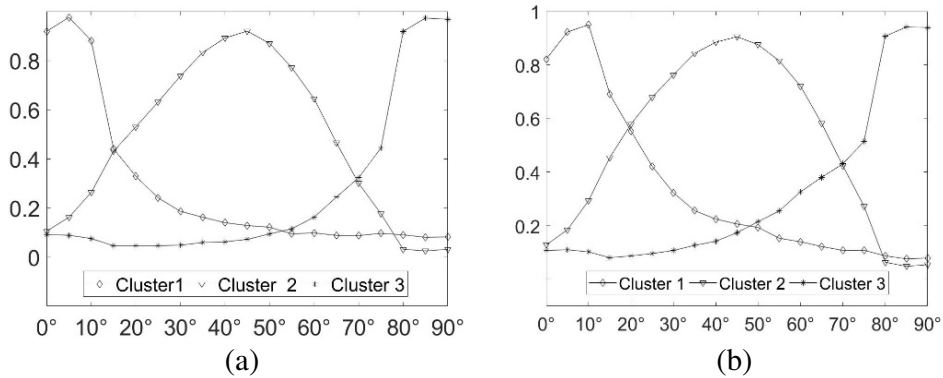


**Figure 10.** Correlation coefficients of the clustering results. (a) Elevation angle 0°; (b) Elevation angle 30°.

coefficients between the cluster center image and the coarse resolution images are given in Figs. 10(a) and (b), respectively. It could be seen from these figures that the scattering behaviors of the illuminated targets vary dramatically among the 3 classes but barely changed within the same group.

Based on the above investigation results and numerical simulation experience, we finally divide the wide-angle observation aperture to 3 sub-apertures. The 3 sub-images are coherently added to help formulate the initialized image according to Eq. (7), where the aspect angle and the corresponding images are given in Figs. 11(a)–(c) and Figs. 12(a)–(c), respectively. The finally derived imageries with elevation angles 0° and 30° are given in Fig. 11(f) and Fig. 12(f), respectively. It could also be seen from Fig. 11(e) and Fig. 12(e) that the resolution of the imagery derived by GLRT method is limited by the observation intervals of sub-apertures, while the real scattering intervals of the illuminated targets might exceed. In comparison, the resolution and interpretability of the imagery reconstructed via our method are both improved since the whole aperture data are utilized, and the actual scatter behaviors are employed in the sparse-based processing.
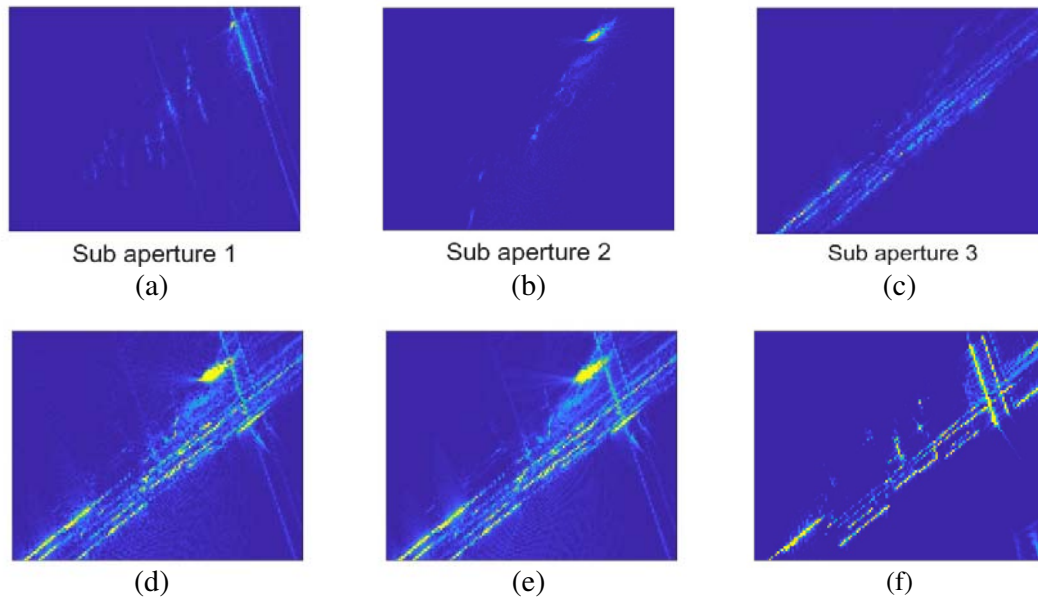
**Figure 11.** Imaging results of Backhoe data with elevation angle 0°. (a), (b) and (c) Imageries of the decomposed sub-apertures; (d) MF; (e) GLRT; (f) Our method.
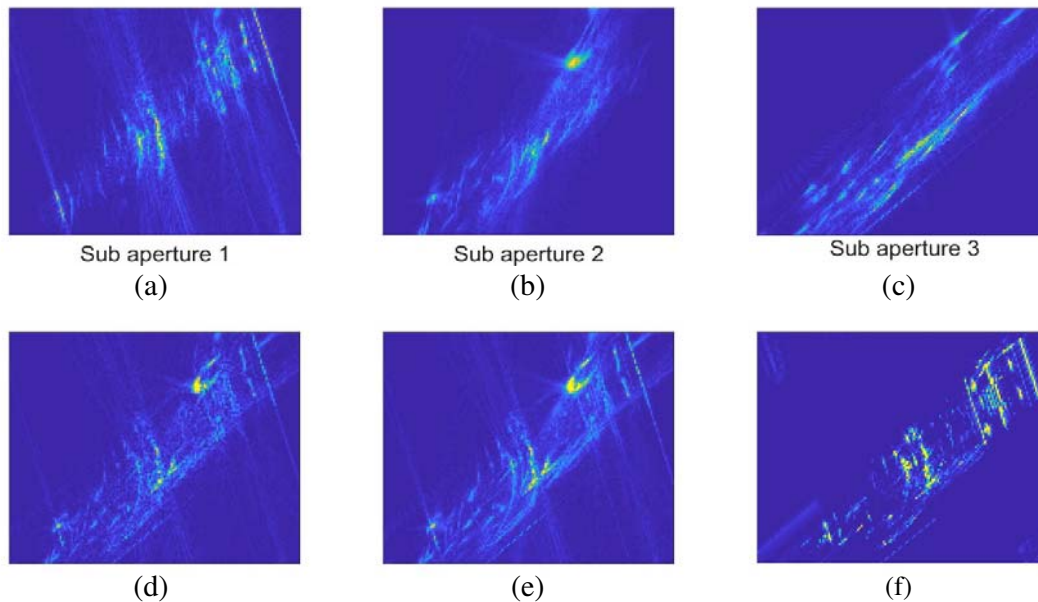


**Figure 12.** Imaging results of Backhoe data. (a), (b) and (c) Imageries of the decomposed sub-apertures; (d) MF; (e) GLRT; (f) Our method.

## 6. CONCLUSION

A sparse-based imaging method for the anisotropic scattering targets is proposed in this paper. Based on the utilization of sparse constraint and scattering amplitude weighting, the mix-received SAR data are separated and reconstructed to obtain two separate images with high focal quality. The resolution and interpretability of the reconstructed imagery are both improved significantly. Numerical simulations verify the validity of the presented methodology.

## ACKNOWLEDGMENT

## REFERENCES

1. Curlander, J. C. and R. N. McDonough, *Synthetic Aperture Radar*, Wiley, New York, 1991.
2. Casteel, Jr., C. H., L. A. Gorham, M. J. Minardi, et al., "A challenge problem for 2D/3D imaging of targets from a volumetric data set in an urban environment," *Proc. SPIE, Algorithms for Synthetic Aperture Radar Imagery XIV*, Vol. 6568, 65680D-1–65680D-7, 2007.
3. Damini, A., B. Balaji, C. Parry, et al., "A video SAR mode for the X-band wideband experimental airborne radar," *Proc. SPIE*, Vol. 7699, 76990E, 2010.
4. Franceschetti, G., R. Lanari, V. Pascazio, et al., "WASAR: A wide-angle SAR processor," *IET Proceedings F Radar & Signal Processing*, Vol. 139, No. 2, 107–114, 2002.
5. Dungan, K. E., J. N. Ash, J. W. Nehrbass, et al., "Wide angle SAR data for target discrimination research,"*Proc. SPIE*, Vol. 8394, 83940M, 2012.
6. Kim, A. J., J. W. Fisher, and A. SWillsky, "Detection and analysis of anisotropic scattering in SAR data," *Multidimensional Systems and Signal Processing*, 49–82, 2003.
7. Ash, J., E. Ertin, L. C. Potter, et al., "Wide-angle synthetic aperture radar imaging: Models and algorithms for anisotropic scattering," *IEEE Signal Processing Magazine*, Vol. 31, No. 4, 16–26, 2014.
8. Trintinalia, L. C., R. Bhalla, and H. Ling, "Scattering center parameterization of wide-angle backscattered data using adaptive Gaussian representation," *IEEE Transactions on Antennas and Propagation*, Vol. 45, No. 11, 1664–1668, 1997.
9. Ferro-Famil, L., A. Reigber, E. Pottier, et al., "Scene characterization using subaperture polarimetric SAR data," *IEEE Transactions on Geoscience and Remote Sensing*, Vol. 41, No. 10, 2264–2276, 2003.
10. Cetin, M. and R. L. Moses, "SAR imaging from partial-aperture data with frequency-band omissions," *Defense & Security International Society for Optics and Photonics*, 2005.
11. Ash, J., E. Ertin, L. Potter, et al., "Wide-angle synthetic aperture radar imaging: Models and algorithms for anisotropic scattering," *IEEE Signal Processing Magazine*, Vol. 31, No. 4, 16–26, 2014.
12. Damini, A., B. Balaji, C. Parry, et al., "A video SAR modefor the X-band wideband experimental airborne radar," *Proc. SPIE*, Vol. 7699, 76990E, 2010.
13. Zuo, F., R. Min, Y. Pi, et al., "Improved method of video synthetic aperture radar imaging algorithm," *IEEE Geoscience & Remote Sensing Letters*, Vol. 16, No. 6, 1–5, 2019.
14. Mosesa, R. L., L. C. Pottera, and M. Cetinb, "Wide angle SAR imaging," *Proc. SPIE 5427, Algorithms for Synthetic Aperture Radar Imagery XI*, 5427, 2004.
15. Iervolin, P., R. Guida, and P. Whittaker, "A new GLRT-based ship detection technique in SAR images," *IEEE IGARSS*, 2015.
16. Çetin, M. and W. C. Karl, "Feature-enhanced synthetic aperture radar formation based on nonquadratic regularization," *IEEE Transactions on Image Processing*, Vol. 10, No. 4, 623–631, 2001.
17. Ertin, E., L. C. Potter, and R. L. Moses, "Enhanced imaging over complete circular apertures," *Proc. Asilomar Conf. Signals, Syst. Comput.*, 1580–1584, 2006.
18. Wu, Y., Jr. Munson, and C. David, "Wide angle ISAR passive imaging using smoothed pseudo Wigner-Ville distribution," *Proc. 2001 IEEE Radar Conference*, 363–368, 2001.

19. De Graaf, S. R., "SAR imaging via modern 2-D spectral estimation methods," *IEEE Transactions on Image Processing*, Vol. 7, No. 5, 729–761, 1998.

20. Ziniel, J. and P. Schniter, "Dynamic compressive sensing of time-varying signals via approximate message passing," *IEEE Transactions on Signal Processing*, Vol. 61, No. 21, 5270–5284, 2013.

21. Jiang, C. L., B. C. Zhang, and Z. D. Wang, "Group-sparse complex approximated message passing algorithm for wide angle synthetic aperture radar imaging," *Journal of Electronics & Information Technology*, Vol. 37, No. 8, 1793–1800, 2015.

22. Varshneya, K. R., M. Cetin, W. Fisher, et al., "Joint image formation and anisotropy characterization inwide-angle SAR," *Proc. of SPIE Algorithms for Synthetic Aperture Radar Imagery XIII*, 6237, 2006.

23. Gerry, M. J., L. C. Potter, I. J. Gupta, et al., "A parametric model for synthetic aperture radar measurements," *IEEE Transactions on Antennas and Propagation*, Vol. 47, No. 7, 1179–1188, 1999.

24. Koets, M. A. and R. L. Moses, "Feature extraction using attributed scattering center models on SAR imagery," *SPIE Algorithms for Synthetic Aperture Radar Imagery VI*, 1999.

25. Candes, E. and M. Wakin, "An introduction to compressive sampling," *IEEE Signal Processing Magazine*, Vol. 25, No. 2, 21–30, 2008.

26. Chartrand, R. and V. Staneva, "Restricted isometry properties and nonconvex compressive sensing," *Inverse Problems*, Vol. 24, No. 3, 1–14, 2008.

27. Cetin, M., I. Stojanovic, O. Onhon, et al., "Sparsity-driven synthetic aperture radar imaging: Reconstruction, autofocusing, moving targets, and compressed sensing," *IEEE Signal Processing Magazine*, Vol. 31, No. 4, 27–40, 2014.

28. Gerry, M. J. and L. C. Potter, "A parametric model for synthetic aperture radar measurements," *IEEE Transactions on Antennas and Propagation*, Vol. 47, No. 7, 1179–1188, 1999.

29. Potter, L. C. and D. M. Chiang, "A GTD-based parametric model for radar scattering," *IEEE Transactions on Antennas and Propagation*, Vol. 43, No. 10, 1058–1067, 1995.

30. He, Y., S. Y. He, Y. H. Zhang, et al., "A forward approach to establish parametric scattering center models for known complex radar targets applied to SAR ATR," *IEEE Transactions on Antennas and Propagation*, Vol. 62, No. 12, 6192–6205, 2014.